Efficient Carbon Nanotube Sponges Production Boosted by Acetone in CVD-Synthesis

Alejandro J. Cortés-López, Emilio Muñoz-Sandoval, Florentino López-Urías*

División de Materiales Avanzados, IPICYT, Camino a la Presa San José 2055, Lomas 4a sección, San Luis Potosí, S.L.P., 78216, México.

Abstract

A high production of nitrogen-doped carbon nanotube sponges (N-CNS) was obtained at 1020 °C with 4 hours of growth in an aerosol-assisted chemical vapor deposition (AACVD) experiment modified with two independent sprayers feeding the reactor. Sprayer-1 contained a solution made of benzylamine, ferrocene, and thiophene; sprayer-2 contained a solution made of ethanol-acetone, ferrocene, and thiophene. N-CNS were produced with three different acetone concentrations and collected along the reactor. The N-CNS were characterized using scanning electron microscopy (SEM), thermogravimetric analysis (TGA), high resolution transmission electron microscopy (HRTEM), X-ray diffraction (XRD), X-ray photoelectron spectroscopy (XPS), and Raman spectroscopy. The main trends that were found when adding acetone as a precursor are: (1) an increase of the carbon fiber diameters; (2) favored the formation of Fe_3C nanoparticles that were encrusted into the outermost layers of the carbon fibers; (3) a reduction of the oxidation temperature; and (4) a decrease in the oxygen content. The nitrogen concentration in N-CNS was approximately 3 % w/w and is exhibited in mainly pyrrolic, pyridinic, and quaternary fashions. The N-CNS showed super hydrophobic and oleophilic properties. The absorption capacities were tested for various organic solvents.

**Correspondence address: flo@ipicyt.edu.mx*

Corresponding author: Tel/Fax: +1 4448342000 (ext. 7238)/+1 4448342010

1. Introduction

Carbon nanotube sponge (CNS) is an interesting material with outstanding properties, such as super hydrophobicity [1], reversible mechanic deformation [2,3], high compressibility [4-6], high absorption capacity [7-8], efficiency for water desalinization [9], being lightweight [10], good conductivity [11], having a large surface area and porosity [12], and high energy dissipation [13]. Due to the high surface area of carbon sponges, they can be used as thermophones [14], super capacitors [6, 15], biosensors [16], electrodes of batteries [17,18], and filters to collect pollutants from water [19]. Chemical vapor deposition (CVD) is an efficient method to produce at large scale carbon nanotubes [20, 21]. The CVD method is a process where volatile precursors are transported to the reactor via the vapor phase, these precursors are decomposed and deposited on a substrate at relative high temperature. Pioneering experiments on the production of the carbon sponges with excellent properties were reported by Gui et al. [1]. They used a CVD method for fabricating their carbon sponges and employed, as precursors, a solution containing ferrocene and 1,2-dichlorobenzene; the carbon sponges grew at 860 °C by 4 h. The carbon sponges exhibited superhydrophobic behavior showing an absorption capacity for oils and organics compounds reached up to ~180 times its own weight. Hashim et al. [22], synthesized boron-doped carbon nanotube sponges at 860 °C using ferrocene, toluene, and triethylborane in an AACVD system. Morphologies of carbon nanotube sponge exhibited entangled network structures with an absorption capacity for organic solvents of ~120 times the sponge's weight. Carbon nanotube sponges doped simultaneously with nitrogen and boron were reported by Zhao et al. [23]. They used ferrocene, toluene, triethylborane, thiophene, and pyridine as precursors in a CVD method at 860 °C. The diameters of the carbon nanotubes were controlled by varying the concentration of the thiophene. Shan et al. [24] synthesized nitrogen-doped carbon nanotube sponges using ferrocene, thiophene, and pyridine in a CVD experiment at 950 °C. They demonstrated that the electrical conductivities of sponges are improved if are formed by carbon nanotubes of small diameters (40-110 nm). Other sponges with astonishing properties that do not only contain carbon nanotubes or fibers have also been produced [25-29]. For

example, Schütt et al. [25] taking as primary architecture a 3D hybrid consisting of a 3D zinc oxide template covered by carbon nanotubes. Then by acid treatment they obtained a novel and excellent functional macroscopic highly porous 3D architectures of interconnected tubes made from self-entangled CNTs, with great potential in polymer applications. Considering the results about a rigid MnO_2-based supercapacitor electrodes [26], Liu and collaborators [27] prepared a remarkable 3D MnO_2@carbon nanotube composite with compressible properties that presented high specific capacitance. By an elegant methodology, Cheng et al. [28] built a superhydrophobic/superoleophilic carbon 3D structure consisting of 4-(heptadecafluorooctyl)aniline-functionalized carbon felts. This novel macroscopic carbon structure also showed good absorption capacity for different organic solvents. Nevertheless the astounding ease approach to build such three-dimensional structures presenting superhydrophobic and superhydrophilic properties, with real possibilities to be used in electrochemical applications, it is also very important to advance in the engineering of 3D carbon nanomaterials, in particular of carbon nanotubes [29]. Lau et al. [30] have been demonstrated that the extraordinary hydrophobic and oleophilic properties of carbon nanotube sponges come from their carbon surface chemical attributes.

The use of alcohols as precursor in CVD method for the production of carbon nanotubes has been reported by different groups [31-37]. For instance, ethanol [31-34], ethanol-methanol [35], ethanol-acetone [36], and acetone [37]. All these studies have demonstrated that the alcohols promote the formation ~~de~~ of long carbon nanotubes with oxygen functionalized groups. Recently, we demonstrated that ethanol can be also used for CNS production [38,39]. However, other organic volatile compounds have not been tested to fabricated 3D carbon structures. Between the most known solvents is the simplest ketone, acetone. This organic compound is decomposed at very low temperatures (~460 °C). It has been demonstrated that using mixtures of ethanol and acetone exhibit differences of critical temperature for the catalytic activity when they are growing on copper [36]. Based on the decomposition temperature of acetone being lower than ethanol (772-807 °C), it is expected that for a high-temperature CVD

experiment (> 800 °C), oxygen and carbon from the acetone will be released as soon as the acetone enters to the reactor, modifying dramatically the catalysis process of carbon nanomaterials.

Here, we report the role of acetone incorporation in the synthesis of nitrogen-doped carbon nanotube networks using a two-sprayer approach in a CVD experiment [39]. Among other things, we demonstrated that acetone increases the production yield and carbon nanotube diameter. The carbon sponge was classified according to where it was grown along the reactor. In the following, the methodology, results, and discussion are presented.

2. Methodology

N-CNS were synthesized using aerosol-assisted chemical vapor deposition (AACVD) with two independent sprayers (sprayer-1 and sprayer-2) feeding the reactor [39]. The synthesis was carried out at 1020 °C over 4 h. The precursors used were benzylamine (Sigma-Aldrich, 99.00 %), ferrocene (Sigma-Aldrich, 98.00 %), thiophene (Sigma-Aldrich, 99.00 %), ethanol (CTR Scientific, 99.70 %) and acetone (CTR Scientific, 99.95 %). The precursor solutions were prepared by varying the ethanol and acetone concentrations. In all solutions, the concentrations of ferrocene and thiophene were kept constant. We prepared four solutions labeled A, B, C, and D. Solution A contains benzylamine, solution B contains ethanol, solutions C contains ethanol-acetone 1:1, and solution D contains ethanol-acetone 1:3. The precursor concentrations used for preparing the different solutions are shown in table 1. Three types of experiments were performed (S1, S2, and S3). In all experiments, sprayer-1 contains solution A. The solution contained in sprayer-2 is varied, for experiment S1, S2, and S3, sprayer-2 contains solutions B, C, and D, respectively.

Both sprayers were connected to quartz tube (length: 90 cm; diameter: 2.54 cm) by a Y-shape glass connecting adapter. The quartz tube was collocated in a tubular furnace (Barnstead Thermolyne Mod.

F21135) with a length of 40 cm. A flow of 1.0 L/min of argon/hydrogen (Infra, 95/5 %) was maintained for sprayer-1, whereas for sprayer-2 a flow of 0.8 L/min of argon (Infra, 99.999 %) was used. Ten samples were collected from three sections by scraping the reactor (initial, middle, and final sections), which were labeled by Mk, k=1-10, and weighed (see figure 1). For instance, M1 (reactor entrance) corresponds to sample collected from 0-5 cm, M2 from 5-10, M3 from 10-15 cm and so on. Thus M9 (40-45 cm) and M10 (45-50 cm) correspond to samples collected outside of the tubular furnace. Samples were characterized by SEM (FEI-Helios NanoLab DualBeam 600 Microscopy), TEM (FEI Tecnai F30). XRD characterizations were performed with a SmartLab X-ray Diffractometer (Rigaku, Co). TGA was carried out using an STA 6000 Perkin-Elmer. Raman spectroscopy characterizations were performed with a Renishaw InVia Confocal Raman Microscope using a laser of wavelength 532 nm. In order to estimate the hydrophobicity, a drop of distilled water was deposited on the surface of N-CNS and the contact angle was measured using a Theta Lite equipment. The following procedure was used to measure the absorption capacity: First, the N-CNS were weighed (Q_0); subsequently, the N-CNS were immersed in the organic solvent for 5 min. Then, the N-CNS were set in contact with absorbent paper to remove the solvent from their surfaces. Finally, the N-CNS containing the solvent were weighed (Q_f). The absorption capacity is defined as $Q = Q_f/Q_0$. Results on absorption capacity are also shown for acid treated N-CNS. Here, the sponges were collocated in a glass and immersed during 1 min in a solution of the HNO_3/H_2SO_4 with a molar relation of 1:3. Then the sponges were washed with distilled water until reaching to pH equal to 7. The sponges were dried at 60 °C for 24 h in a gravity oven Lindberg/Blue-M.

3. Results and discussion

First, we show the N-CNS production yield (table 2). The production yields obtained for experiment S1 (ethanol), S2 (ethanol-acetone 1:1), and S3 (ethanol-acetone 1:3) were 3.460 g, 9.522 g, and 13.425 g, respectively. The increase in the yield production was not absolutely associated with an increase to the amount of N-CNS, other carbon materials emerged as shown below. The incorporation of acetone

derived in a null or negligible production carbon material in some zones depending of the ethanol-acetone mixture (table 2). This fact can be interpreted in terms of the temperature profile along the tubular furnace and the decomposition temperature of the acetone. Figure 2 exhibits the temperature profile and the weight of material obtained by zones along the reactor, indicating clearly that the maximum of yield production is acquired from the high temperature middle zone, with a displacement to the right, when the amount of acetone increases. Since the acetone exhibits a lower decomposition temperature than ethanol, it is expected that oxygen atoms are delivered just at the entrance of the reactor

Figure 3 depicts the SEM images of the carbon structures that were obtained along the reactor; here, one sample per section was chosen (the one with a high yield production). For experiment S1 (figure 3a-c), long and curly carbon fibers with diameters of ~80 nm and ~200 nm dominate in the initial and middle sections, respectively, see figure 3(a-b). At the end of the reactor (final section), the carbon sponges are non-longer formed; instead, the formation of onion-like carbon material which are formed by small nanoparticles of ~2-12 nm diameter surrounded by graphite layers (figure 3c). Details on the structure of this material will be shown ahead. SEM images for experiment S2 are shown in figure 3(d-f). Curly long carbon fibers with ~20 nm diameters were grown at the initial section (figure 3d). At the middle section, large diameter curly entangled carbon fibers were obtained (figure 3e) with different diameters (520-810 nm), see diameter distribution in figure S1. At the final section, carbon fibers with ~60 nm diameters and small iron nanoparticles were grown (figure 3f). Figure 3(h-i) displays the SEM images of experiment S3, showing that short carbon fibers were found at the initial section (figure 3g). At the middle section, entangled carbon fibers of 200-1000 nm diameters dominate the sample (figure 3h and figure S1). At the end of the reactor, we found carbon fibers up to ~3 μm diameter and onion-like carbon material were also observed (figure 3i). In general, entangled curly carbon fibers were grown at the middle section of the reactor with an increased fiber diameter for syntheses with ethanol-acetone. It is important to mention

that for the middle section, we found pieces made of entangled curly carbon fibers with lateral dimensions up to 4 cm.

Figure 4 shows TEM images of carbon fibers that were collected from the middle section of the reactor. A curly carbon fiber is illustrated in figure 4a. This fiber exhibits a core-shell structure, while the core is formed by well-aligned graphite layers, the shell is formed by disordered graphite layers. A high magnification image of the carbon fiber tip shows that the core fiber has an ~62 nm diameter and that nanoparticles of various sizes are attached to the carbon fiber (figure 4b). Figure 4c clearly depicts the well-aligned graphite layers of the core fiber, showing an interlayer distance of ~3.36 Å. The entangled curly carbon fibers, shown in figure 4d, exhibit a bamboo shaped morphology, probably due to the influence of nitrogen [40,42] and sulfur [43,44]. Figure 4e depicts a ~400 nm diameter carbon fiber, which shows the internal or core carbon fiber. Figure 4f shows a carbon fibers. The inset in figure 4f displays a large metal nanowire inside the carbon fiber. HRTEM images, shown in figure 5a, provide additional insight into the structure of the carbon fibers. The carbon fibers have metal nanoparticles anchored on their surfaces and embedded into the graphite layers (figure 5a). The embedded particles give rise to large prolonged cavities along the carbon fiber. Energy-dispersive X-ray spectroscopy (EDX) analysis on such incrusted metal nanoparticles revealed the presence of C and Fe (figure S2a). Figure 5b displays the tip of a carbon fiber and shows the core fiber surrounded by folded graphite layers (see arrow). Figure 5c shows a curly carbon fiber with Fe-based nanoparticles inside. The end of the carbon fiber exhibits a curly structure due to the Fe-based nanoparticles inside (see the inset). Figure 5d shows an HRTEM image of the metal nanoparticle enclosed by the circle in figure 5c, revealing an interlayer distance of 4.54 Å, which is attributed to the (100) crystallographic planes of iron carbide (Fe_3C). Figure 6 displays SEM and HRTEM images of carbon materials obtained at the end of the reactor (final section). The SEM images clearly show the presence of carbon fibers and carbon onion-like material, figure 6(a-

b). HRTEM images of this material revealed that it is composed of metal nanoparticles with ~2-12 nm diameters surrounded by a few graphite layers; EDX analysis on a metal nanoparticle revealed the presence mainly of S, Fe, and C as shown in figure S2(b-c).

Raman spectra of N-CNS are shown in figure 7. The vertical lines refer to the typical values of graphite for the D-band and the G-band. The Raman spectra are similar; however, a thorough analysis of the D- and G-band peak positions revealed upshifts and downshifts of up to 30 cm^{-1}, when compared to graphite. Notice that the D-peak and G-peak positions depend both on where the sponges were collected in the reactor and the acetone concentration. The Raman shifts values for the D- and G-bands are indicated in figure 7d. The D-bands downshift is preferentially observed for samples from experiment S3 (ethanol-acetone 1:3). The D-band downshift is attributed to the presence of structural defects, such as vacancies, edges, and non-hexagonal rings [45]. Regarding the G-band, a downshift is dominant in most samples; the downshift was likely caused by the nitrogen doping [46]. Figure 7e depicts the ratio of the intensity of the D- and G-bands peaks (I_D/I_G). Samples from experiments S2 and S3 exhibited the largest values of I_D/I_G, suggesting the presence of structural defects.

XRD characterizations of N-CNS are displayed in figure 8. The vertical line refers to the standard position for graphite. The peak of the (002) crystallographic plane, typical of graphite materials, follows interesting trends. In our case, asymmetric and wide peaks can be observed for samples synthesized at the middle section of the reactor (samples M4, M5, M6, and M7). This asymmetry suggests the presence of at least two distinct interlayer distances. A deconvolution of the (002) graphite peaks provides information on the graphitization degree of the N-CNS. Many factors could affect the graphitization degree such as positive or negative curvatures of the graphene layers, presence of functional groups at edges, generation of vacancies, and doping [47]. The conventional graphite and turbostratic graphite possess a regular spacing but different stacking, while convectional graphite possess ABAB stacking,

turbostratic graphite is randomly stacked. According to XRD, the (002) crystallographic plane provides information about stacking of graphene layer over c-direction and how growth the stacked in that direction. For instance, Singh et al [48] realized a peak profile fit using two Voigt spectral functions to process (002) peak and identify the crystalline structures related. The information obtained indicated that interlayer distances increase with nanotube diameter producing a displacement in (002) peak, such displacement also could be associated to curvature of the graphene layers. They discovered that with increment of the diameter of the nanotubes the FWHM decrease and the component in 2θ is gradually is modified as increase or decrease the distance of the graphene layers. In our case, the (002) peak was fitted using two pseudo-voigt curves to fit the peaks (π and γ curves). In figure S3 (Supplementary Information), we show an example of a deconvoluted peak. The interlayer distances derived from the π and γ curves (dπ(002) and dγ(002)) are shown in tables S(1-3). The area under the π curve provides information on the degree of graphitization of the sample. Figure 8d depicts the interlayer distance and the percentage area under the π and γ curves. Samples synthesized with acetone exhibited the largest values of dπ(002), see figure 8d. Regarding the dγ(002), the largest values were obtained for samples from experiments S1 and S2, suggesting the likely presence of turbostratic graphite or embedded small Fe-based nanoparticles in the graphite layers (figure 8e). Figure S3 (Supplementary Information) depicts the XRD plots showing the signals of the catalytic nanoparticles for 2θ=32-90.

The TGA results for the N-CNS revealed interesting trends (figure 9). Here, the TGA provides information on the amount of Fe content and the thermal stability of the N-CNS. The sample weight versus temperature curve showed different behaviors depending on where the samples were collected in the reactor. The oxidation temperatures were in the ranges of 630-647 °C, 541-650 °C, and 517-656 °C for the initial (figure 9a), middle (figure 9b), and final (figure 9c) sections, respectively. These oxidation temperatures are lower than the obtained for functionalized few-walled carbon nanotube sponge (~700

°C) [49], higher than the carbon foams case (~400°C) [50], and similar to the graphite oxide situation (~650 °C) [51]. The lowest oxidation temperatures were found for sample S1-M8 from the final section. For the middle section, where production yield is high, the N-CNS produced with ethanol-acetone 1:3 are less thermally stable (sample S3-M6, figure 9b), showing an oxidation temperature of 541 °C. In table 3, we summarize the weight of the residual materials and the oxidation temperatures.

XPS characterizations for samples that were collected from the middle section. The XPS survey spectra revealed the presence of Si, C, N, and O whose concentrations are sensitive to the concentration of acetone, see figure 10 and table S4. The N-CNS produced with acetone exhibited lower oxygen concentrations, 2.9-3.8 % w/w. Samples synthesized with only ethanol showed the highest oxygen content of 6.3 % w/w. All considered samples exhibited nitrogen concentrations of 3.5-4.9 % w/w, which are larger than those of nitrogen-doped carbon nanotubes produced with the benzylamine and ferrocene precursors [40]. The deconvoluted C1s, N1s, and O1s peaks are shown in figure 11. The binding energies (gravity center), full width at half maximum (FWHM), and integrated area of the expanded peaks are shown in tables S(5-7) in Supplementary Information. The expanded C1s peak analysis (table S5) revealed the presence of C=C, C-C, C-O and O-C=O chemical species, see figure 11(a-c). The C=C bonds are related to sp^2 aromatic carbon rings. The C-C bonds can be associated to sp^3 hybridization. The C-O and O-C=O bonds are attributed to chemical groups attached to the sponge surface or edges. Since the N-CNS are super hydrophobic, we believe that these oxygen functional groups do not correspond to phenolic or carboxylic groups, which are hydrophilic groups. Likely these functional groups could be part of esters (methyl or ethyl acetate) and ethers (methoxy and ethoxy) these organic species exhibit a methyl radical ($-CH_3$), which is non-polar and hydrophobic, at their tails. The expanded N1s peak, see figure 11(d-f), reveals that the nitrogen is incorporated via N-quaternary, N-pyrrolic, and N-pyridinic into the graphite layers, see also table S6. Traces of N-O bonds were detected in all samples. Amine group ($-NH_2$) signals were observed for N-CNS that were synthesized with a high acetone

concentration (figure 11f). Recently, Shan et al. [24] used ferrocene and pyridine as precursors in a CVD experiment to dope carbon nanotube sponges, they reached up to 4.3 % of nitrogen content being N-quaternary the main specie found in their carbon sponges. In our case, we observed that the pyrrolic is dominant in N-CNS synthesized with ethanol, whereas the N-quaternary is favored when the acetone is incorporated in the reaction. Notice that the reactivity of the nitrogen doping at carbon lattice is an important research field due to nitrogen doping is related with possible practical applications. For instance, pyridinic–type nitrogen atoms could improve of the electrochemical activity of the electrodes based in carbon material [53]. For the expanded O1s peak, traces of O_2/C, COOH, N-O, Fe-O, and Fe(OH)O were identified, see figure 11(g-i) and table S7.

The hydrophobicity of the spongy materials were tested by putting a colored water drop on the N-CNS's surfaces, figure 12(a-c). A highly hydrophobic behavior, which maintained the surface tension and spherical shape of water droplets was kept on the N-CNS surface. We measured a contact angle of ~142° which is in accord with previous studies [38]. In our carbon nanotube sponges, the high hydrophobicity could be related to the roughness of the material or the presence of water-fearing chemical groups (ether- and ester-groups) which exhibit alkyl radical bonded to carbonyl groups [38].

The absorption capacity properties of N-CNS are shown in figure 12(d-f). The results for samples S1-M4 (figure 12d), S2-M5 (figure 12e), and S3-M7 (figure 12f) were obtained. N-CNS that were synthesized using only ethanol yielded better results, reaching Q values of 30 and 45 times its weight for the ethylene-glycol and dichlorobenzene, respectively (figure 12d). The N-CNS produced by incorporating acetone in the CVD method exhibited a reduction of the absorption capacity, as shown in figure 12(e-f). Notice that our absorption capacities are lower than obtained by Gui et al. [1], they found absorptions up to ~125 times their weight for mineral oil using densities of carbon sponges of ~7.0 $mg.cm^{-3}$.

Figure 13 shows a preliminary study on the role of the acid treatment on the absorption capacity of our carbon sponges. Here, the N-CNS were exposed to an acid treatment for one minute, which caused severe structural damage, see SEM images in figure 13(a-d). The carbon sponges become hydrophilic with a lower absorption capacity for organic solvents. The absorption capacities of acid treated N-CNS are shown in figure 13(e-g). The oil absorption capacity decreased possibly due to the steric impediment of the amorphous carbon with functional groups decreasing the affinity to create Van der Walls or electrostatics interactions with organic solvents. Also as the superhydrophobicity is related with the oil absorption capacity [52], it is possibly that acid treatment formed more oxygenated groups, losing the superhydrophobicity behavior and becoming partially hydrophilic. Acid treatment in N-CNS causes a negative effect on their absorption properties, however, more investigation in this direction is needed.

4 Conclusions

The XPS characterizations revealed the presence of oxygen functional groups, suggesting the anchoring of ethoxy and ester groups on the surface of the N-CNS. We found that carbon fibers exhibited inner ordered graphite layers (~40 nm diameter) and outer layers with poor graphitization (~20 nm thickness). We have also found metal-nanoparticles with an α-Fe, γ-Fe and Fe_3C composition inside, embedded, and on the surface of the carbon fibers. TGA revealed that the N-CNS present oxidation temperatures from 600 to 700 °C. The N-CNS were tested for hydrophobicity and organic solvents absorption, which demonstrated that they are super hydrophobic with interesting solvent absorption properties; they absorbed up to 45 times their own weight. The absorption capacity measurements using methanol, gasoline, vacuum oil, vegetable oil, diesel, ethylen-glycol, dichlorobenzene, and chloroform as solvents demonstrated that N-CNS produced with only ethanol are better absorbers than those produced with ethanol-acetone mixtures. The main effects of the acetone in N-CNS production were: (1) an increase of the coaxial carbon nanotube diameter; (2) a greater amount of material in the middle area; (3) the

inclusion of Fe_3C nanoparticles in the body of N-CNS; (4) increasing of reactivity of N-CNS due to the decrease of oxidation point; (5) increase of oxygenated chemical groups on the surface of N-CNS; (6) Surprising changes in the surface of the N-CNS due to short time acid treatment have also been shown. Spongy material mixed with other carbon species, which were grown mainly at the inlet and outlet of the reactor, is also present. However, although the N-CNS is found at the middle part, the real spongy material grows shifted to the right with the increasing of acetone. Carbon nanotube sponges are a novel and fascinating macroscopic material whose individual constituents are of nanoscopic size; that exceptional findings is far that be ended. Research to discover more of these new carbon materials with surprising physical and chemical properties as well as to find more efficient applications are in progress. This work contains relevant results that concern new ways of creating carbon 3D-nanomaterials with novel properties that could be also used for ionic batteries.

Author contributions

E.M.S. and F.L.U. designed the research and wrote the manuscript. A. J. C. L. conducted the experiments, analyzed the data, reviewed the manuscript and wrote the manuscript.

Competing financial interests

The authors declare no competing financial interests.

Acknowledgments

EMS thanks CONACYT for Grant CB-2013-220744. The authors thank LINAN and IPICYT for the characterization facilities, as well as M.Sc. Beatriz A. Rivera-Escoto, Dr. Gladis J. Labrada-Delgado, M.Sc. Ana Iris Peña-Maldonado, Dr. Héctor G. Silva-Pereyra, M.Sc Dulce Partida-Gutiérrez, and Dr. Mariela Bravo-Sánchez.

References

[1]. Gui, X.; Wei, J.; Wang, K.; Cao, A.; Zhu, H.; Jia, Y.; Shu, Q.; Wu, D. Carbon Nanotube Sponges. *Adv. Mater.* 2010, 22, 617-621.

[2]. Gui, X.; Zeng, Z.; Cao, A.; Lin, Z.; Xiang, R.; Wu, T.; Zhu, Y.; Tang, Z. Elastic Shape Recovery of Carbon Nanotube Sponges in Liquid Oil. *J. Mater. Chem.* 2012, 22, 18300-18305.

[3]. Li, P.; Kong, C.; Shang, Y.; Shi, E.; Yu, Y.; Qian, W.; Wei, F.; Wei, J.; Wang, K.; Zhu, H.; Cao, A.; Wu, D. Highly Deformation-Tolerant Carbon Nanotube Sponges as Supercapacitor Electrodes. *Nanoscale* 2013, 5, 8472-8479.

[4]. Gui, X.; Cao, A.; Wei, J.; Li, H.; Jia, Y.; Li, Z.; Fan, L.; Wang, K.; Zhu, H.; Wu, D. Soft, Highly Conductive Nanotube Sponges and Composites with Controlled Compressibility. *ACS Nano* 2010, 4(4), 2320-2330.

[5]. Xue, Y.; Yang, Y.; Sun, H.; Li, X.; Wu, S.; Cao, A.; Duan, H. A Switchable and Compressible Carbon Nanotube Sponge Electrocapillary Imbiber. *Adv. Mater.* 2015, 27, 7241-7246.

[6]. Li, P.; Shi, E.; Yang, Y.; Shang, Y.; Peng, Q.; Wu, S.; Wei, J.; Wang, K.; Zhu, H.; Yuan, Q.; Cao, A.; Wu, D. Carbon Nanotube–Polypyrrole Core–Shell Sponge and its Application as Highly Compressible Supercapacitor Electrode. *Nano Research* 2014, 7(2), 209-218.

[7]. Gui, X.; Li, H.; Wang, K.; Wei, J.; Jia, Y.; Li, Z.; Fan, L.; Cao, A.; Zhu, H.; Wu, D. Recyclable Carbon Nanotube Sponges for Oil Absorption. *Acta Mater.* 2011, 59, 4798-4884.

[8]. Gao, Y.; Zhou, Y. S.; Xiong, W.; Wang, M.; Fan, L.; Rabiee-Golgir, H.; Jiang, L.; Hou, W.; Huang, X.; Jiang, L.; Silvain, J. F.; Lu, Y. F. Highly Efficient and Recyclable Carbon Soot Sponge for Oil Cleanup. *ACS Appl. Mater. Interfaces* 2014, 6, 5924-5929.

[9]. Wang, L.; Wang, M.; Huang, Z.H.; Cui, T.; Gui, X.; Kang, F.; Wang, K.; Wu, D. Capacitive Deionization of NaCl Solutions Using Carbon Nanotube Sponge Electrodes. *J. Mater. Chem.* 2011, 21, 18295-18299.

[10]. Crespo, M.; González, M.; Elías A.L.; Rajukumar, L.P.; Baselga, J.; Terrones, M.; Pozuelo, J. Ultra-light Carbon Nanotube Sponge as an Efficient Electromagnetic Shielding Material in the GHz Range. *Phys. Status Solidi* 2014, 8(8), 298-704.

[11]. Zhong, J.; Yang, Z.; Mukherjee, R.; Thomas A.V.; Zhu, K.; Sun, P.; Lian, J.; Zhu, H.; Koratkar, N. Carbon Nanotube Sponges as Conductive Networks for Supercapacitor Devices. *Nano Energy* 2013, 2, 1025–1030.

[12]. Li, H.; Gui, X.; Zhang L.; Wang, S.; Ji, C.; Wei, J.; Wang, K.; Zhu, H.; Wu, D.; Cao, A. Carbon Nanotube Sponge Filters for Trapping Nanoparticles and Dye Molecules from Water. *Chem. Commun.* 2010, 46, 7966–7968.

[13]. Gui, X.; Zeng, Z.; Zhu, Y.; Li, H.; Lin, Z.; Gan Q.; Xiang, R.; Cao, A.; Tang, Z. Three-Dimensional Carbon Nanotube Sponge-Array Architectures with High Energy Dissipation. *Adv. Mater.* 2014, 26, 1248–1253.

[14]. Aliev, A. E.; Mayo, N. K.; de Andrade, M. J.; Robles, R. O.; Fang, S.; Baughman, R. H.; Zhang, M.; Chen, Y.; Lee, J. A.; Kim, S. J. Alternative Nanostructures for Thermophones. *ACS Nano* 2015, 9(5), 4743-4756.

[15]. Chen, W.; Rakhi, R. B.; Hu, L.; Cui, Y.; Alshareef, H. N. High-Performance Nanostructured Supercapacitors on a Sponge. *Nano Lett.* 2011, 11, 5165-5172.

[16]. Li, Y.; Zhao, M.; Chen, J.; Fan, S.; Liang, J.; Ding, L.; Chen, S. Multifunctional Biosensor Based on Self-Assembled Multi-Walled Carbon Nanotubes Sponge. *J. Mater. Sci. Mater. Electron.* 2016, 27(7), 6911-6917.

[17]. Shen, Y.; Sun, D.; Yu, L.; Zhang, W.; Shang, W.; Shang, Y.; Tang, H.; Wu, J.; Cao, A.; Huang, Y. A High-Capacity Lithium–Air Battery with Pd Modified Carbon Nanotube Sponge Cathode Working in Regular Air. *Carbon* 2013, 62, 288-295.

[18]. Sharifi, T.; Valvo, M.; Gracia-Espino, E.; Sandström, R.; Edström, K.; Wagber, T. Hierarchical Self-Assembled Structures Based on Nitrogen-Doped Carbon Nanotubes as Advanced Negative Electrodes for Li-Ion Batteries and 3D Microbatteries. *J. Power Sources* 2015, 279, 581-592.

[19]. Li, H.; Gui, X.; Zhang, L.; Wang, S.; Ji, C.; Wei, J.; Wang, K.; Zhu, H.; Wu, D.; Cao, A. Carbon Nanotube Sponge Filters for Trapping Nanoparticles and Dye Molecules From Water. *Chem. Commun.* 2010, 46, 7966-7968.

[20]. Cassell, A.M.; Raymakers, J.A.; Kong J.; Da,i H.; Large Scale CVD of Single-Walled Carbon Nanotubes. *J. Phys. Chem.* 1999, 103, 6484-6492.

[21]. Couteau, E.; Hernadi, K.; Seo, J.W.; Thien-Nga, L.; Mikó, Cs.; Gaál, R.; Forró, L. CVD synthesis of high-purity multiwalled carbon nanotubes using $CaCO_3$ catalyst support for large-scale production. *Chem. Phys. Lett.* 2003, 278, 9-17.

[22]. Hashim, D.P.; Narayanan, N.T.; Romo-Herrera, J.M.; Cullen, D.A.; Hahm, M.G.; Lezzi, P.; Suttle, J.R.; Kelkhoff, D.; Muñoz-Sandoval, E.; Ganguli, S.; Roy, A.; Smith, D.J.; Vajtai, R.; Sumpter, B.G.; Meunier, V.; Terrones, H.; Terrones, M.; Ajayan, P.M. Covalently Bonded Three-Dimensional Carbon Nanotube Solids Via Boron Induced Nanojunctions. *Sci. Rep.* 2012, 2, 363.

[23]. Zhao, W.; Shan, C.; Elias, A.L.; Rajukumar, L.P.; O'Brien, D.J.; Terrones, M.; Wei, B.; Suhr, J.; Lu, X.L. Hyperelasticity of Three-Dimensional Carbon Nanotube Sponge Controlled by the Stiffness of Covalent Junctions. *Carbon* 2015, 95, 640-645.

[24]. Shan, C.; Zhao, W.; Lu, X.L.; O'Brien, D.J.; Li, Y.; Cao, Z.; Elias, A.L.; Cruz-Silva, R.; Terrones, M.; Wei, B.; Suhr, J. Three-Dimensional Nitrogen-Doped Multiwall Carbon Nanotube Sponges with Tunable Properties. *Nano Lett.* 2013, 13, 5514-5520.

[25]. Schütt, F.; Signetti, S.; Krüger, H.; Röder, S.; Smazna, D.; Kaps, S.; Gorb, S.N.; Mishra, Y. K.; Pugno, N.M.; Adelung, R. Hierarchical self-entangled carbon nanotube tube networks. *Nat. Comm.* 2017, 8, 1215.

[26]. Choi, C. S., Sim, H. J., Spinks, G. M., Lepró, X., Baughman, R. H., Kim, S. J. Supercapacitors: Elastomeric and Dynamic MnO_2/CNT Core–Shell Structure Coiled Yarn Supercapacitor. *Adv. Energy Mater.* 2016, 6, 1502119.

[27]. Liu, Y.; Zhou, X.; Liu, R.; Li, X.; Bai, Y.; Yuan, G. Preparation of three-dimensional compressible MnO_2@carbon nanotube sponges with enhanced supercapacitor performance. *New J. Chem.* 2017, 41, 14906.

[28]. Cheng, Y.; He, G.; Barras, A.; Coffinier, Y.; Lu, S.; Xu, W.; Szunerits, S.; Boukherroub, R. One-step immersion for fabrication of superhydrophobic/superoleophilic carbon felts with fire resistance: Fast separation and removal of oil from water. *Chem. Eng. J.* 2018, 331, 371-382.

[29]. Dasgupta, A., Pulickal Rajukumar, L., Rotella, C., Lei, Y., Terrones, M. Covalent three-dimensional networks of graphene and carbon nanotubes: synthesis and environmental applications. *Nano Toda*y 2017, 12, 116–135.

[30]. Lau, K.K.S.; Bico, J.; Teo, K.B.K.; Chhowalla, M.; Amaratunga, G.A.J.; Milne, W.I.; McKinley, G.H.; Gleason, K.K. Superhydrophobic Carbon Nanotube Forest. *Nano Lett.* 2003, 3 (12) 1701-1705.

[31]. Huang L., Cui X., White B., O'Brien S.P. Long and Oriented Single-Walled Carbon Nanotubes Grown by Ethanol Chemical Vapor Deposition. *The Journal of Physical Chemistry B 2004*, 108, 16451-16456.

[32]. Buang N.A., Ismail F., Athoman M.Z. Synthesis of Carbon Nanotube Heterojunctions from the Decomposition of Ethanol. *Fullerenes, Nanotubes, and Carbon Nanostructures* 2014, 22, 307-315.

[33]. Li Y.L., Zhang L.H., Zhong X.H., Windle A.H. Synthesis of high purity single-walled carbon nanotubes from ethanol by catalytic gas flow CVD reactions. *Nanotechnology* 2007, 18 225604.

[34]. A. Botello-Méndez, J. Campos-Delgado, A. Morelos-Gómez, M. A. Vidal, H. Navarro, H. Terrones, M. Terrones. Controlling the dimensions, reactivity and crystallinity of multiwalled carbon nanotubes using low ethanol concentrations. *Chem. Phys. Lett.* 453 (2008) 55.

[35]. Qi H., Qian C., Liu J. Synthesis of High-Purity Few-Walled Carbon Nanotubes from Ethanol/Methanol Mixture. *Chemistry of Materials* 18 (2006) 5691-5695.

[36]. Peng X., Koczkur K., Chen A. Synthesis of well-aligned bamboo-like carbon nanotube arrays from ethanol and acetone. *Journal of Physics D: Applied Physics* 41 (2008) 095409 (6pp).

[37]. Melezhik A.V., Smykuv M. A., Filatova E. Y., Shuklinov A.V., Stolyarov R.A., Larionova I.S., Tkachov A.G. Synthesis of Carbon Nanotubes from Acetone. *Theoretical Foundations of Chemical Engineering* 2013 47 (4), 435-443.

[38]. Muñoz-Sandoval, E.; Cortés-López, A.J.; Flores-Gómez, B.; Fajardo-Díaz, J.L.; Sánchez-Salas, R.; López-Urías, F. Carbon Sponge-Type Nanostructures Based on Coaxial Nitrogen-Doped Multiwalled Carbon Nanotubes Grown by CVD Using Benzylamine as Precursor. *Carbon* 2017, 115, 409-421.

[39]. Muñoz-Sandoval, E.; Fajardo-Díaz, J.L.; Sánchez-Salas, R.; Cortés-López, A.J.; López-Urías, F. Two Sprayer CVD Synthesis of Nitrogen-doped Carbon Sponge-type Nanomaterials. *Sci. Rep.* 2018, 8, 2983.

[40]. Czerw, R.; Terrones, M.; Charlier, J.C.; Blasé, X.; Foley, B.; Kamalakaran, R.; Grobert, N.; Terrones, H.; Tekleab, D.; Ajayan, P.M.; Blau, W.; Rühle, M.; Carroll, D.L. Identification of Electron Donor States in N-doped Carbon Nanotubes. *Nano Lett.* 2001, 1(9), 457-460.

[41]. Ewels, C. P.; Glerup, M. Nitrogen Doping in Carbon Nanotubes. *J. Nanosci. Nanotechnol.* 2005, 5, 1345-1363.

[42]. Maldonado, S.; Morin, S.; Stevenson K.J. Structure, Composition, and Chemical Reactivity of Carbon Nanotubes by Selective Nitrogen Doping. *Carbon* 2006, *44*, 1429-1437.

[43]. Romo-Herrera, J. M.; Sumpter, B. G.; Cullen, D. A.; Terrones, H.; Cruz-Silva, E.; Smith, D.J.; Meunier, V.; Terrones, M. An Atomistic Branching Mechanism for Carbon Nanotubes: Sulfur as the Triggering Agent. *Angew. Chem. Int. Ed.* 2008, *47*, 2948-2953.

[44]. Romo-Herrera, J. M.; Cullen, D. A.; Cruz-Silva, E.; Ramírez, D.; Sumpter, B.G.; Meunier, S.V.; Terrones, H.; Smith, D.J.; Terrones, M. The Role of Sulfur in the Synthesis of Novel Carbon Morphologies: From Covalent Y-Junctions to Sea-Urchin- Like Structures. *Adv. Funct. Mater.* 2009, *19*, 1193-1199.

[45]. Dresselhaus, M.S.; Dresselhaus, G.; Saito, R.; Jorio, A. Raman Spectroscopy of Carbon Nanotubes. *Phys. Rep.* 2005, *409*, 47-99.

[46]. Ferrari, A.C.; Basko, D.M. Raman Spectroscopy as a Versatile Tool for Studying the Properties of Graphene. *Nat. Nanotechnol.* 2013, *8*, 235-246.

[47]. Li Z.Q., Lu C.J., Xia Z.P., Zhou Y., Luo Z. X-ray diffraction patterns of graphite and turbostratic carbon. *Carbon* 45, 1686-1695 (2007).

[48]. Singh D.K., Iyer P.K., Giri P.K. Diameter dependence of interwall separation and strain in multiwalled carbon nanotubes probed by X-ray diffraction and Raman scattering studies. *Diamond & Related Materials 2010*, 19, 1281-1288.

[49]. Jeon, I.Y.; Choi, J.I.; Lee, S.G.; Chae, H.G.; Jang, S.S.; Kumar, S.; Baek, J.B. Sponge Behaviors of Functionalized Few-Walled Carbon Nanotubes. *J. Phys. Chem.* 2010, 114, 14868-14875.

[50]. Xiao, N.; Zhou, Y.; Ling, Z.; Zhao, Z., Qiu, J. Carbon foams made of in situ produced carbon nanocapsules and the use as a catalyst for oxidative dehydrogenation of ethylbenzene. *Carbon* 2013, 60, 514-522.

[51]. Jeong, H.K.; Lee, Y.P.; Jin, M.H.; Kim, E.S.; Bae, J.J; Lee, Y.H. Thermal stability of graphite oxide. *Chem. Phys. Lett.* 2009, 470, 244-258.
[52]. Zhang, Y.; Stan, L.; Xu, P.; Wang, H. L.; Doom, S.K.; Htoon, H.; Zhu, Y.; Jia, Q. A double-layered carbon nanotube array with super-hydrophobicity. Carbon 2009, 47, 3332-3336.
[53]. Rao, C. V.; Cabrera, C.R.; Ishikawa, Y. In Search of the Active Site in Nitrogen-Doped Carbon Nanotube Electrodes for the Oxygen Reduction Reaction. *J. Phys. Chem. Lett.* 2010, 1, 2622-2627.

TABLES AND CAPTIONS

Table 1: Alejandro J. Cortés-López et al.

Solution*	Precursors	Concentration (wt%)
A	Benzylamine	97
	Ferrocene	2.5
	Thiophene	0.5
B	Ethanol	98.6
	Ferrocene	1.28
	Thiophene	0.128
C	Ethanol-Acetone (1:1)	98.6
	Ferrocene	1.28
	Thiophene	0.128
D	Ethanol-Acetone (1:3)	98.6
	Ferrocene	1.28
	Thiophene	0.128

* 500 mL were prepared of each solution.

Table 1: Content of the solutions that were used as precursors in the aerosol assisted chemical vapor deposition (AACVD) experiment; two sprayer configuration, see figure 1. In all experiments, sprayer-1 contained solution A. The content of sprayer-2 was varied between the B, C, and D solutions for experiments S1, S2, and S3, respectively.

Table 2: Alejandro J. Cortés-López et al.

Section	Label	Range (cm)	Weight (g)		
			Ethanol (S1)	**Ethanol-Acetone 1:1 (S2)**	**Ethanol-Acetone 1:3 (S3)**
Initial	M1	0-5	0.019	-----	-----
	M2	5-10	0.315	1.518	1.839
	M3	10-15	1.538	-----	-----
Middle	M4	15-20	1.089	3.226	-----
	M5	20-25	0.106	1.808	-----
	M6	25-30	0.206	1.431	4.619
	M7	30-35	0.104	0.778	3.160
Final	M8	35-40	0.083	0.560	3.165
	M9	40-45	-----	0.201	0.302
	M10	45-50	-----	-----	0.340
		Total	**3.460**	**9.522**	**13.425**

Table 2: Yield production samples obtained in the AACVD experiment and classified based on their position along the reactor (quartz tube). Notice that an increase of the acetone concentration promotes an increase in the yield production of carbon material (experiments S2 and S3). The spongy carbon material formed mainly by tangled carbon fibers was obtained in middle section.

Table 3: Alejandro J. Cortés-López et al.

Section	Sample	Temperature (°C)	Residual materials (%)
Initial	S1-M3	647	0.000
	S2-M2	640	3.14
	S3-M2	630	3.14
Middle	S1-M4	635	2.69
	S2-M4	650	0.000
	S3-M6	541	1.570
Final	S1-M8	517	25.34
	S2-M8	656	0.00125
	S3-M8	572	0.00249

Table 3: Oxidation temperatures and residuals from TGA for the N-CNS collected along the reactor (initial, middle, and final sections). A high amount of residue was obtained for experiment S1 (ethanol precursor) at the final section.

FIGURES AND CAPTIONS

Figure 1: Alejandro J. Cortés-López et al.

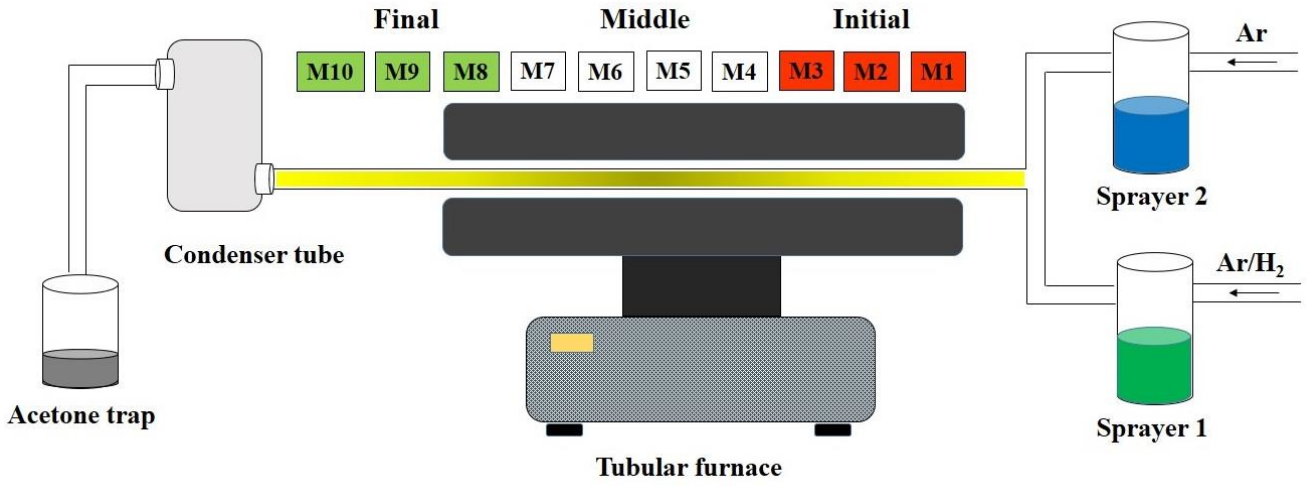

Figure 1: Schematic representation of the aerosol assisted chemical vapor deposition (AACVD) setup, showing the two sprayer configuration (sprayer-1 and sprayer-2). Sprayer-1 contains a solution of ferrocene, benzylamine, and thiophene, whereas sprayer-2 contains ferrocene, ethanol, acetone and thiophene. Details on the different concentrations can be seen in table 1. The samples are collected and labeled by Mk (k=1,…, 10), according to their position along the reactor.

Figure 2: Alejandro J. Cortés-López et al.

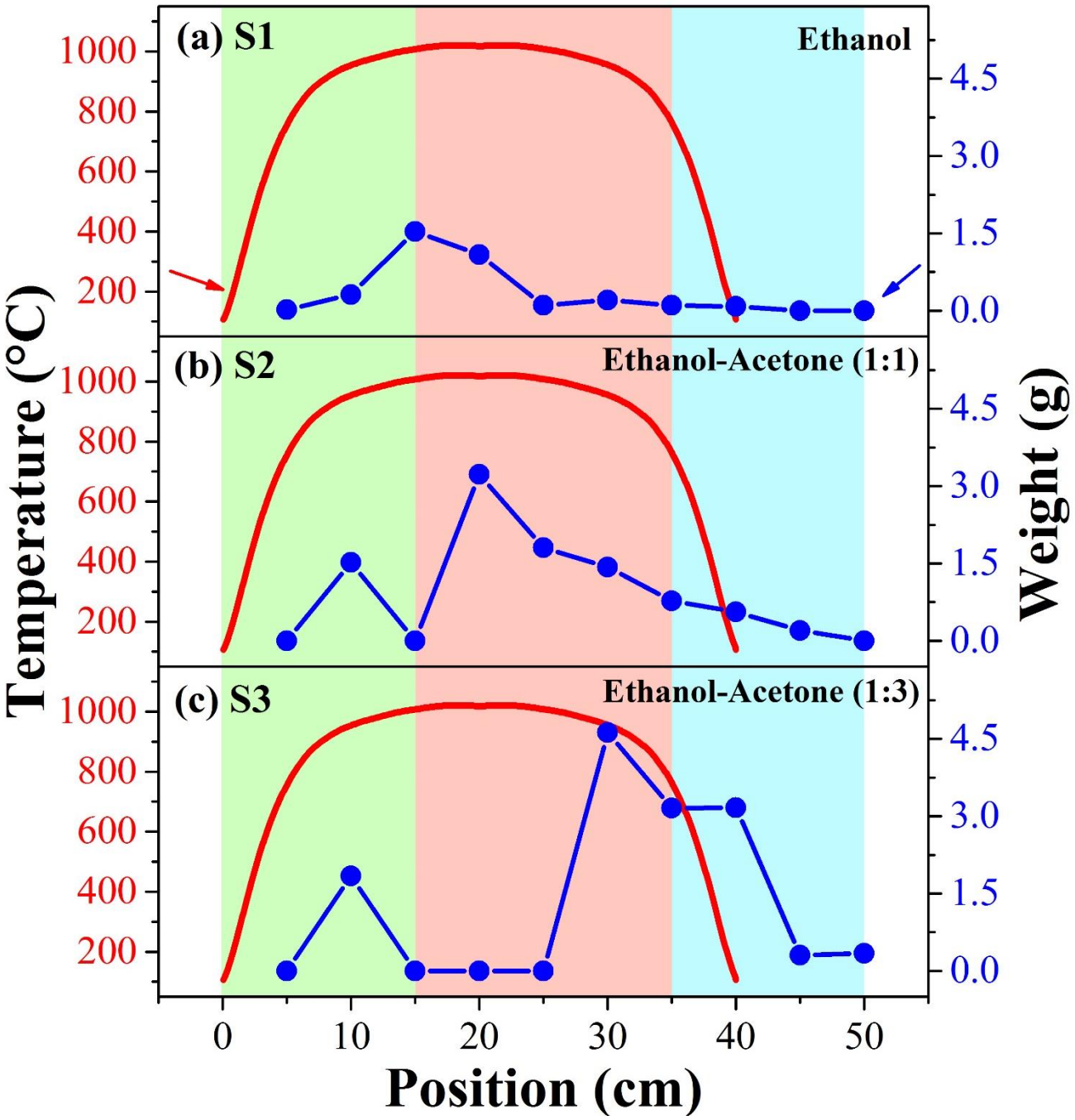

Figure 2: Temperature profile in the tubular furnace and yield production of carbon materials alongside the reactor. The N-CNS were obtained mainly in the middle section, from 15-35 cm.

Figure 3: Alejandro J. Cortés-López et al.

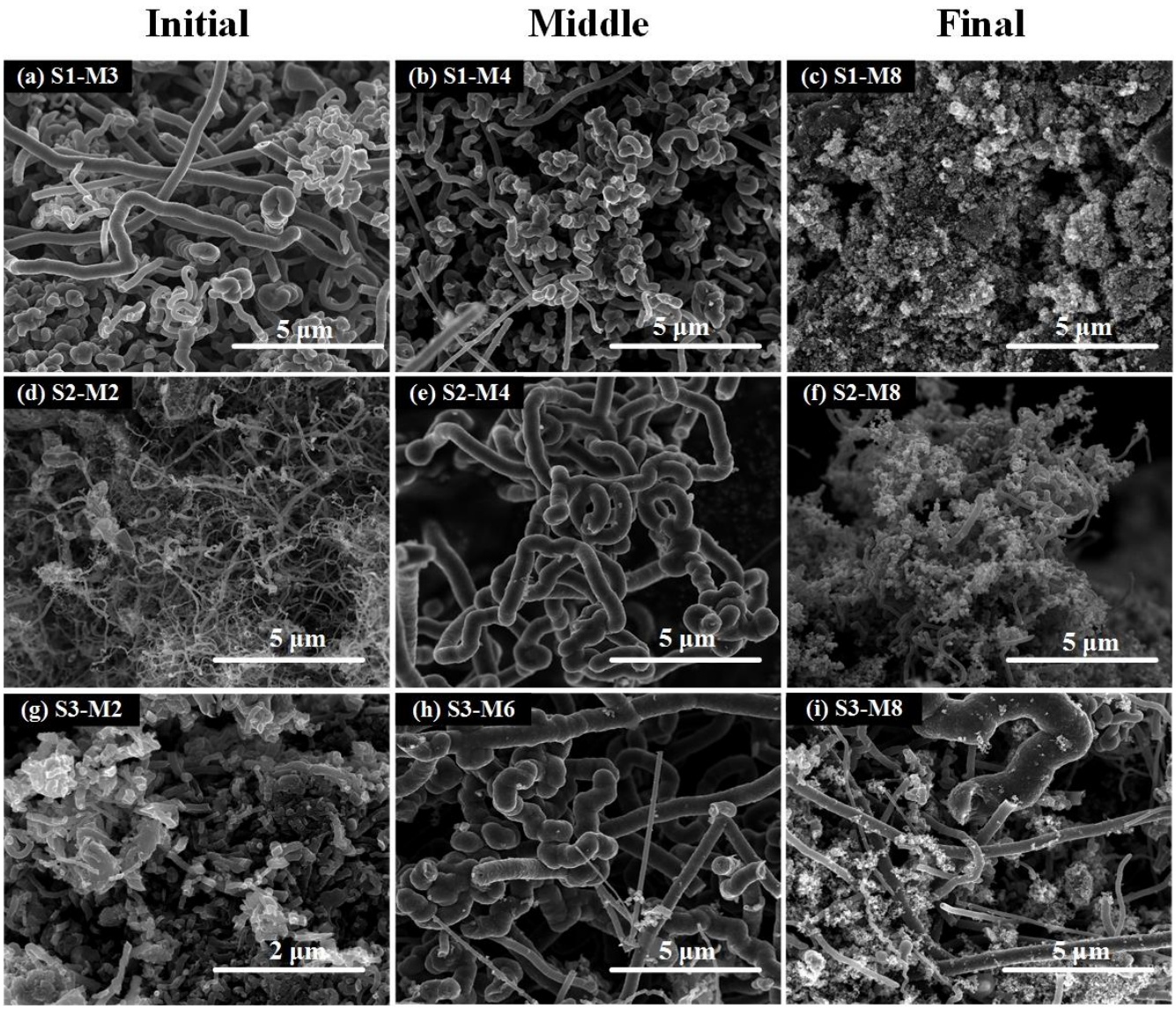

Figure 3: SEM images showing the N-CNS synthesized along the reactor for experiments S1 (first row), S2 (second row), and S3 (third row). Images displayed in the second column, which were obtained from

the middle section in the reactor, correspond to well-entangled carbon nanofibers (spongy carbon material). Different diameters (520-810 nm) can be observed. The diameter distribution can be seen in figure S1.

Figure 4: Alejandro J. Cortés-López et al.

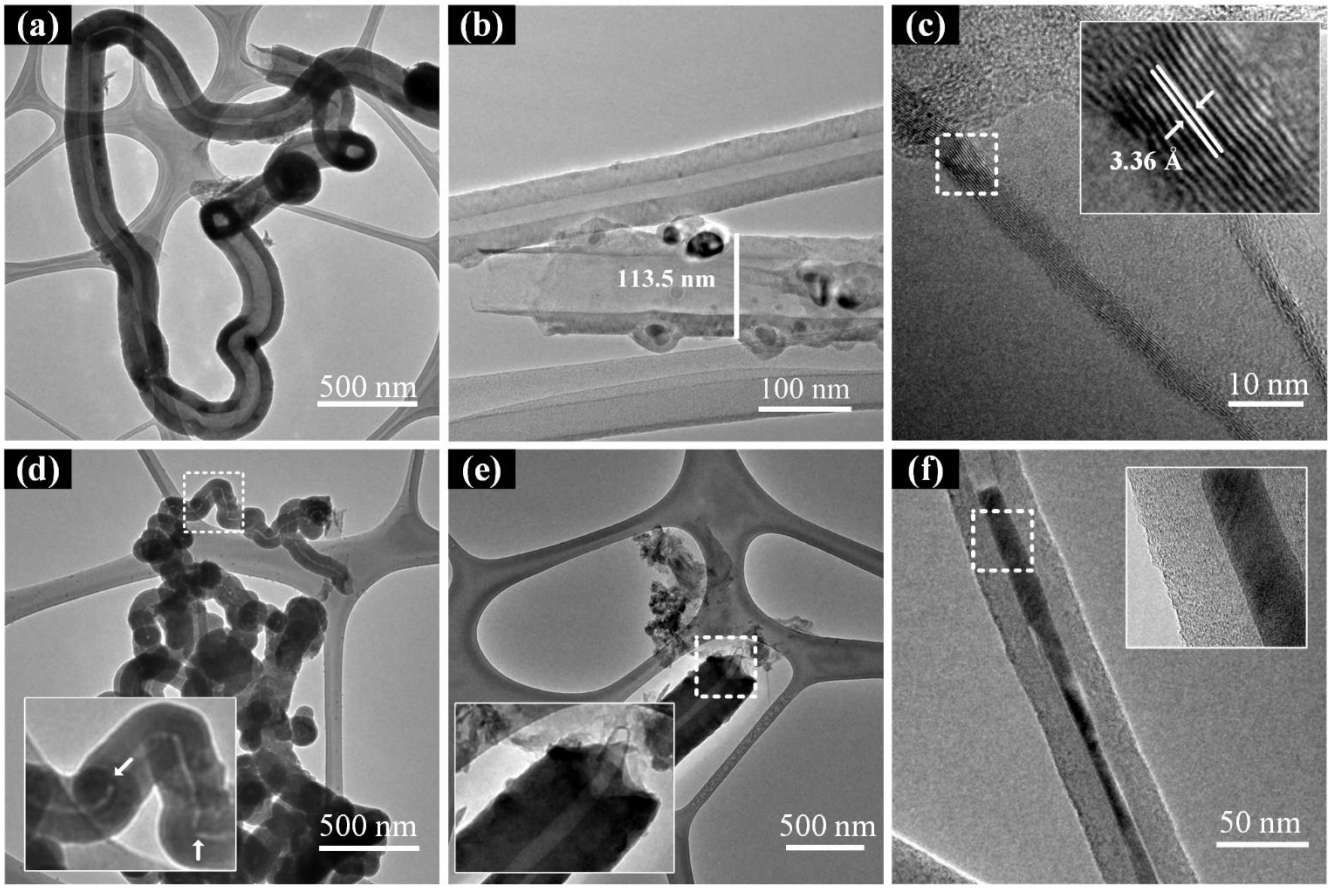

Figure 4: TEM images of N-CNS. **(a)** Curly carbon nanotubes, **(b)** tip of a curly carbon nanotube. **(c)** Inter-planar spacing of graphite layers in the inside MWCNT carbon nanotube. **(d)** Curly carbon nanotubes with a bamboo shape, see the inset. **(e)** Carbon fiber showing a few layer MWCNT inside. **(f)** Carbon nanotube with iron compound inside. **(a)-(c)** From experiment S1, **(d)-(e)** from experiment S2, **(f)** from experiment S3.

Figure 5: Alejandro J. Cortés-López et al.

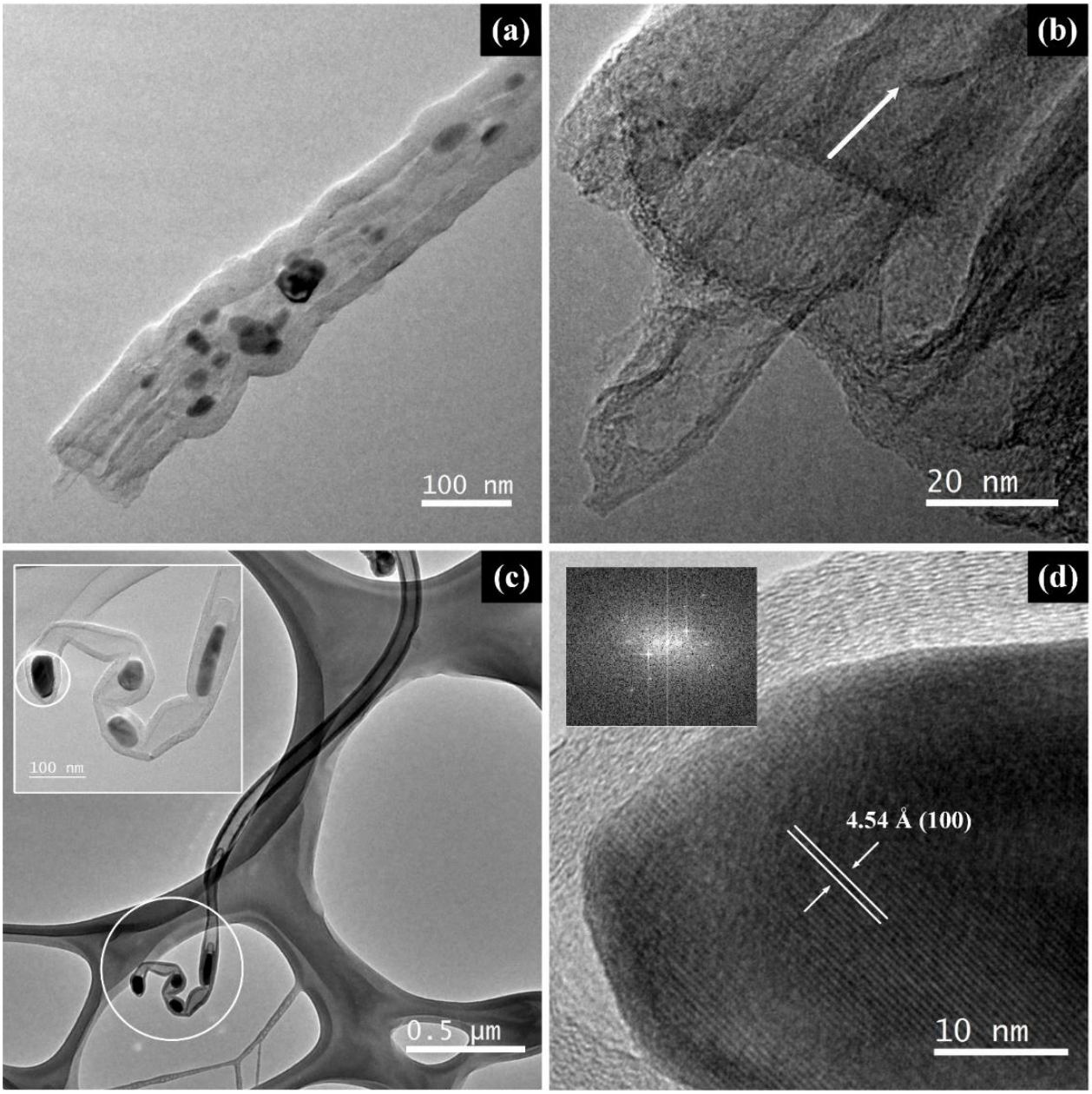

Figure 5: HRTEM images of carbon nanotubes with particles inside and embedded. **(a)** Multiwalled carbon nanotube with iron carbide nanoparticles inside. **(b)** High magnification of the graphite tip from image **(a)**. **(c)** Long carbon nanotube with Fe_3C nanoparticles inside (see the enclosed area). **(d)** Fe_3C nanoparticle surrounded by graphite layers, exhibiting an interplanar distance of 4.54 Å corresponding to (100) crystallographic planes.

Figure 6: Alejandro J. Cortés-López et al.

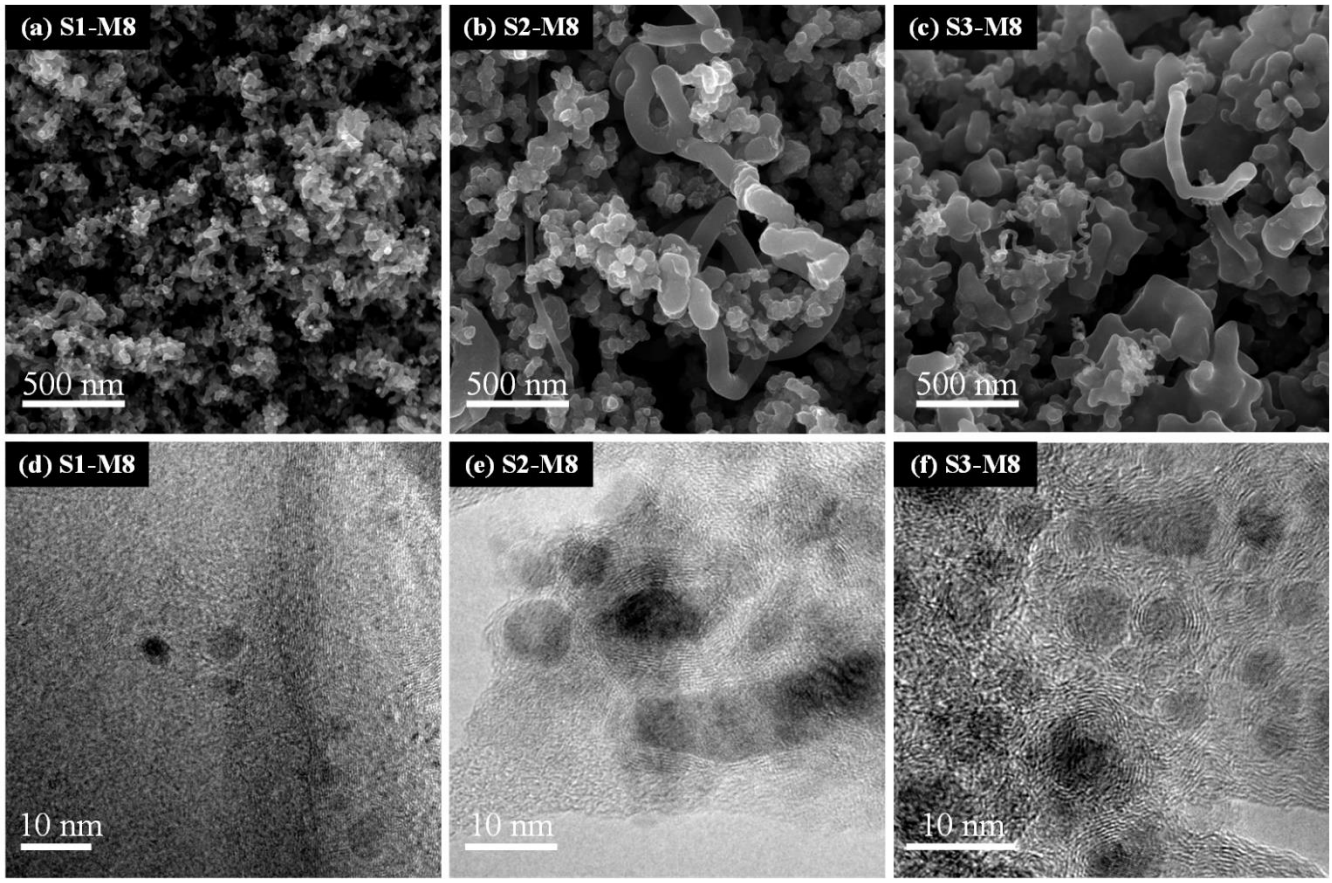

Figure 6: (a)-(c) SEM images of nanoparticles distributed in the final section from experiments S1, S2, and S3. **(d)-(f)** The corresponding HRTEM images. The sponge contains carbon fibers and onion-like carbon materials formed by metal nanoparticles surrounded by graphite layers.

Figure 7: Alejandro J. Cortés-López et al.

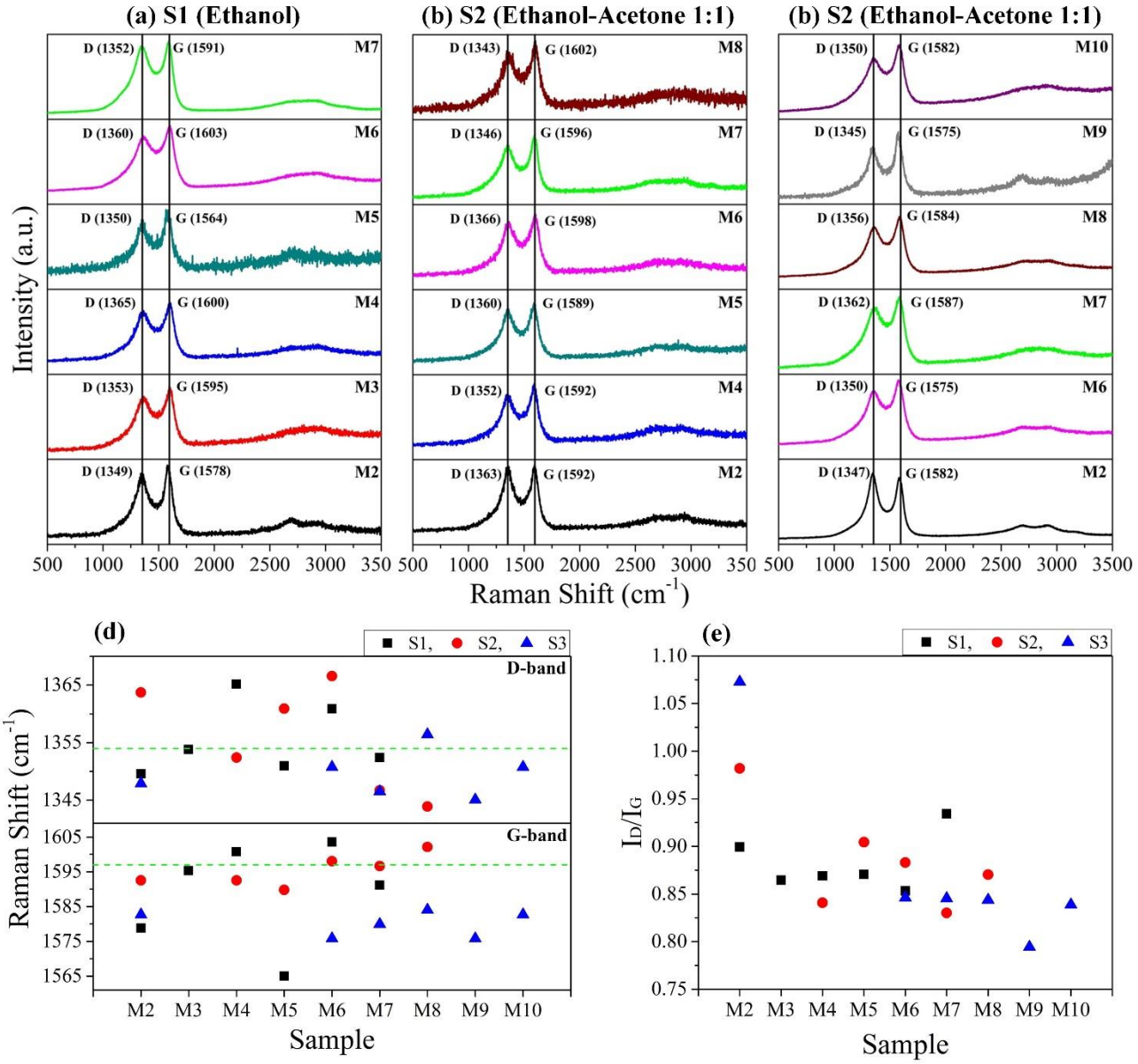

Figure 7: Raman characterization of N-CNS materials. **(a)** Samples S1 (synthesized using only ethanol), **(b)** samples S2 (synthesized using ethanol-acetone 1:1), and (**c)** sample S3 (synthesized using ethanol-acetone 1:3). The vertical lines indicate the typical values of D and G Raman shift in graphite. The label M indicates where the samples were collected in the reactor. **(d)** The D and G band values. The green dashed lines indicate the D and G graphite bands with values of 1354 and 1597 cm^{-1}, respectively. **(e)** The ratio of the intensity of the D- Raman peak and the G- Raman peak (I_D/I_G).

Figure 8: Alejandro J. Cortés-López et al.

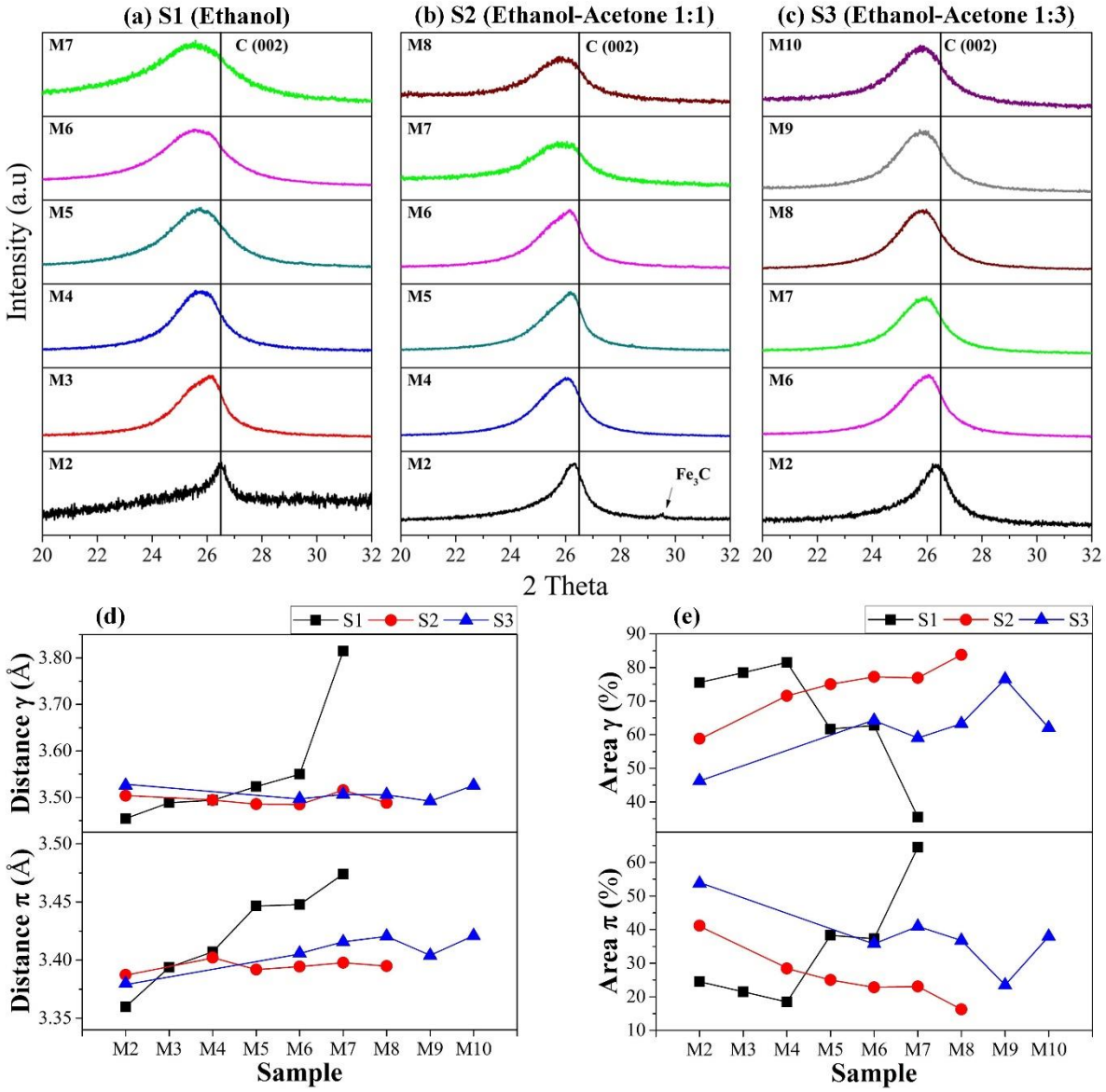

Figure 8: XRD plots for 2θ=20-32 showing the (002) crystallographic plane, typical of graphitic materials. **(a)** Experiment S1, **(b)** experiment S2, and **(c)** experiment S3. The vertical lines indicate the standard values for graphite. The label M indicates where the samples were collected along the reactor. **(d)** The interplanar spacing (dπ and dγ) was derived from the gravity center of the Gaussian curves. **(e)** Area under the Gaussian curves. Large values of the area (π) is an indication of a high degree of

graphitization. XRD plots for 2θ=32-90 can be seen in figure S4, revealing the presence of iron and iron carbide nanoparticles.

Figure 9: Alejandro J. Cortés-López et al.

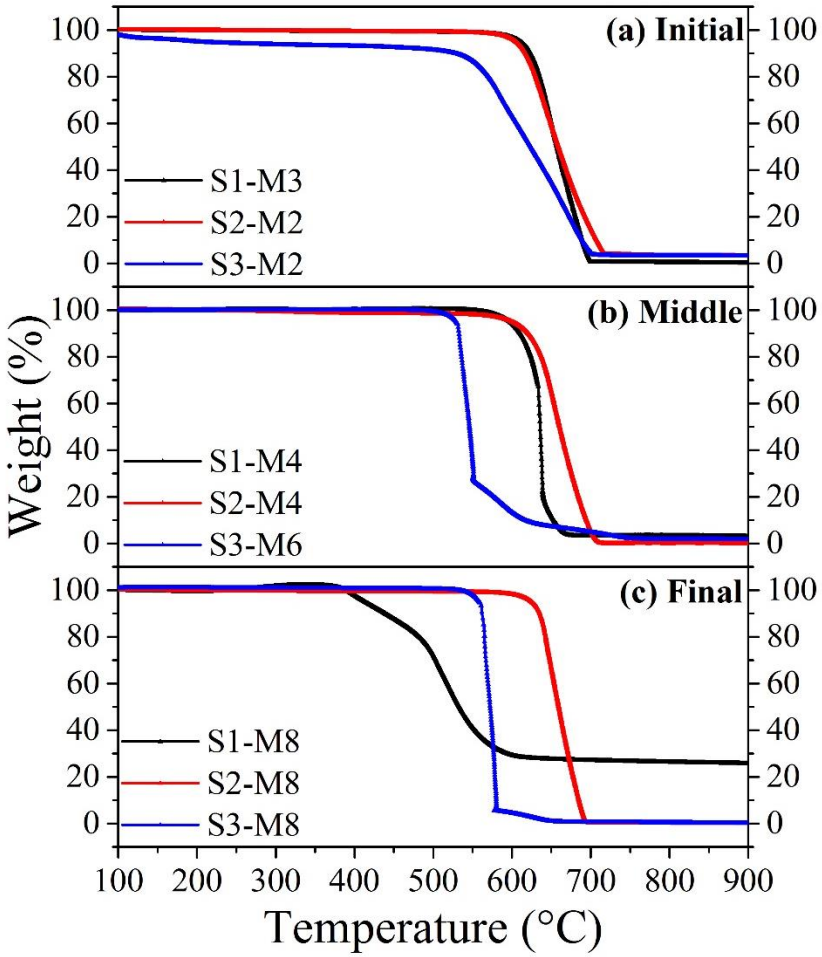

Figure 9: TGA analysis of N-CNS from experiment S1, S2 and S3 for **(a)** initial, **(b)** middle and **(c)** final sections. The corresponding morphologies can be seen in figure 2. The oxidation temperatures and residual weights are shown in table 3. The highest residual weight was found for S1-M8 (sample collected from the final section).

Figure 10: Alejandro J. Cortés-López et al.

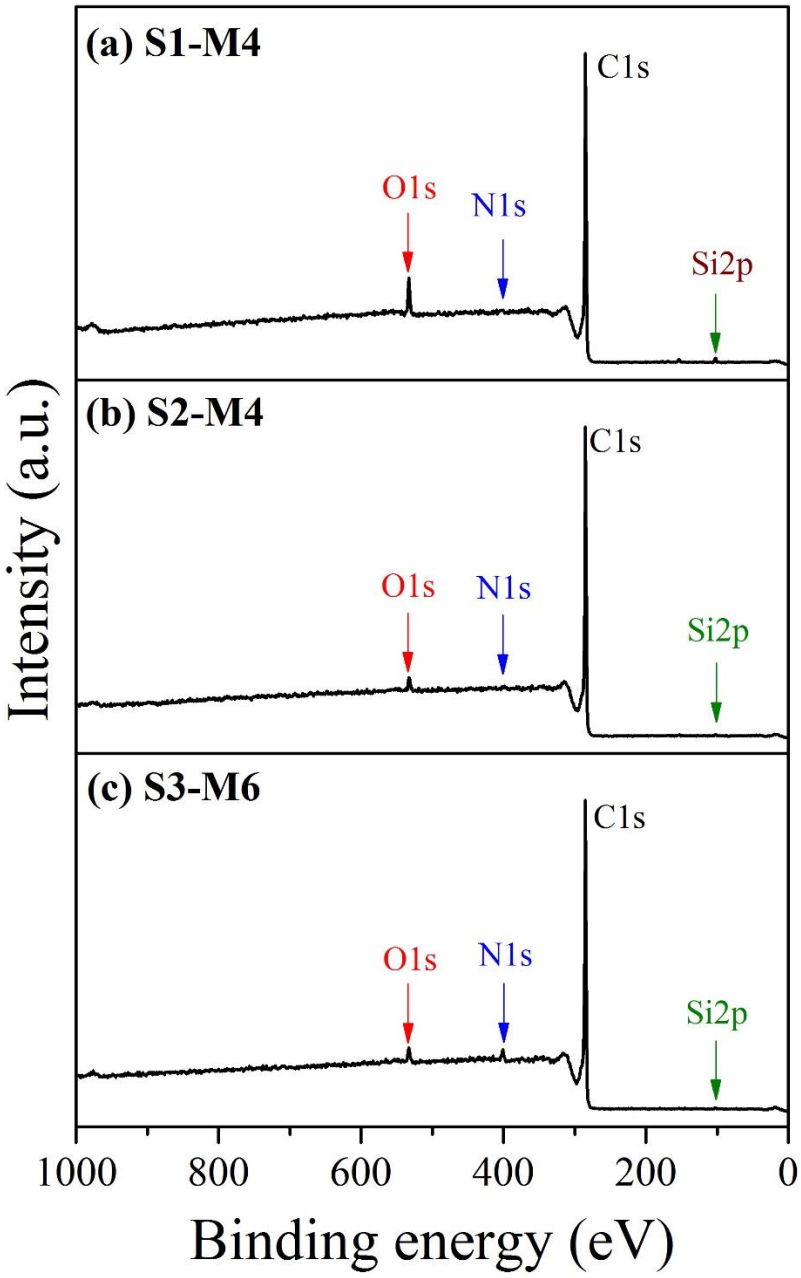

Figure 10: XPS survey of N-CNS. **(a)** S1-M4, **(b)** S2-M4 and **(c)** S3-M6. Atomic percent can be seen in table SI-4.

Figure 11: Alejandro J. Cortés-López et al.

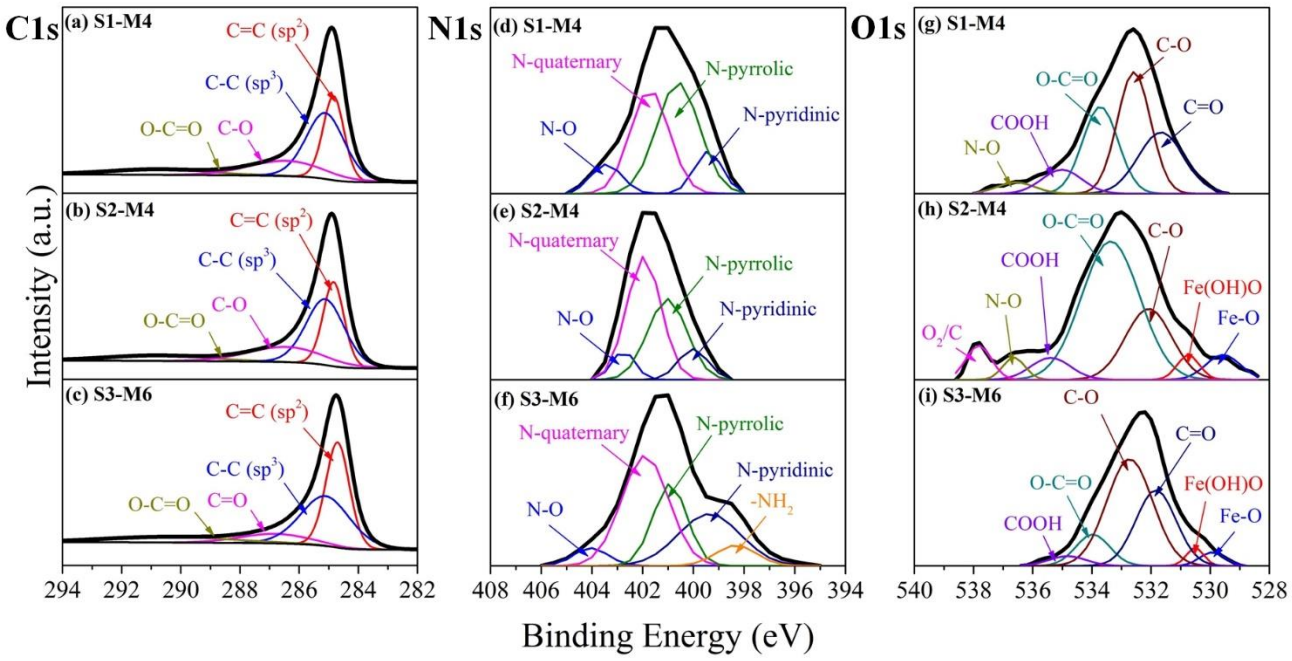

Figure 11: XPS analysis for the expanded C1s, N1s and O1s peaks for N-CNS obtained at the middle section of the reactor. **(a,d,g)** S1-M4, **(b,e,h)** S2-M4, and **(c,f,i)** S3-M6. Details on the deconvolution analysis are shown in table SI-5-7 (Supplementary Information).

Figure 12: Alejandro J. Cortés-López et al.

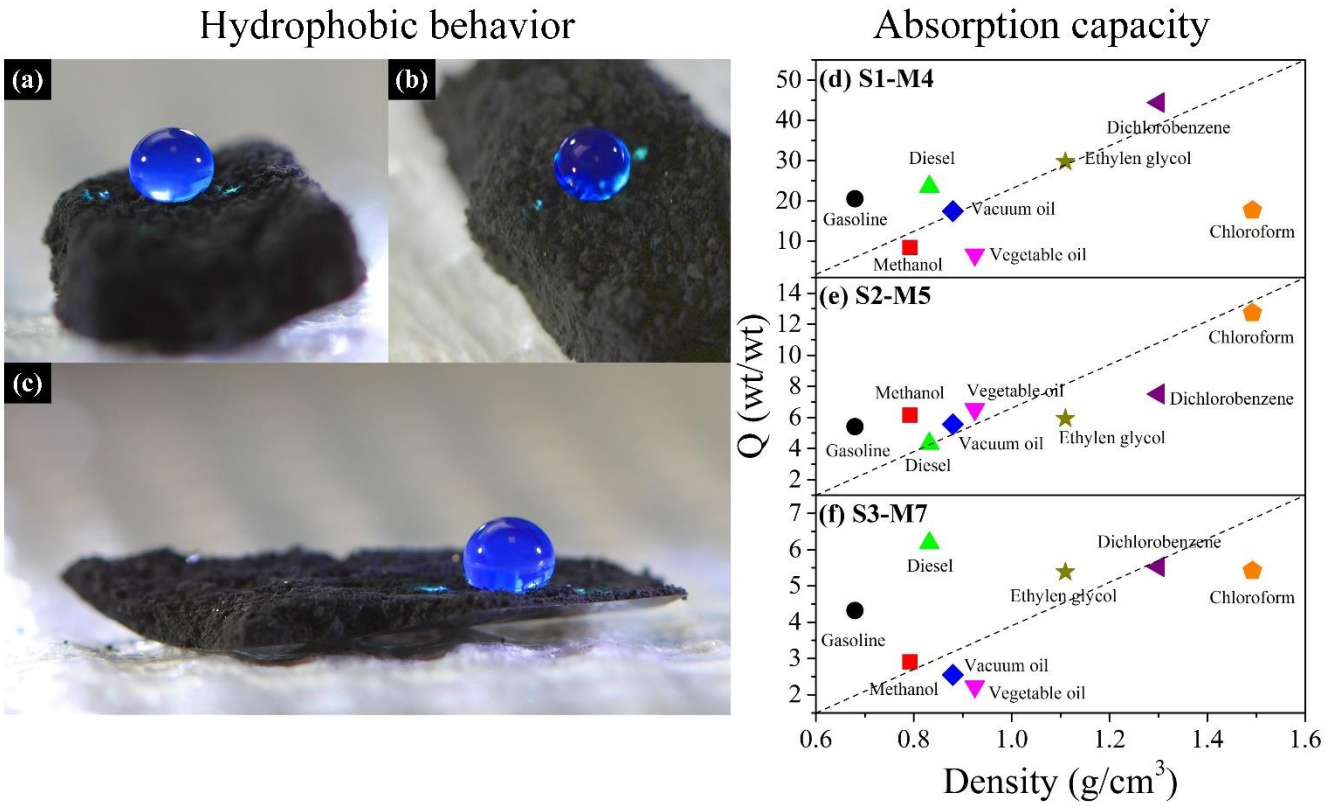

Figure 12: Images of water droplets demonstrating the hydrophobic behavior with surface contact angle > 150°, **(a)** and **(b)** N-CNS from experiment S1, **(c)** N-CNS from experiment S2. Solvents absorption properties for **(d)** S1-M4, **(e)** S2-M5, and **(f)** S3-M7.

Figure 13: Alejandro J. Cortés-López et al.

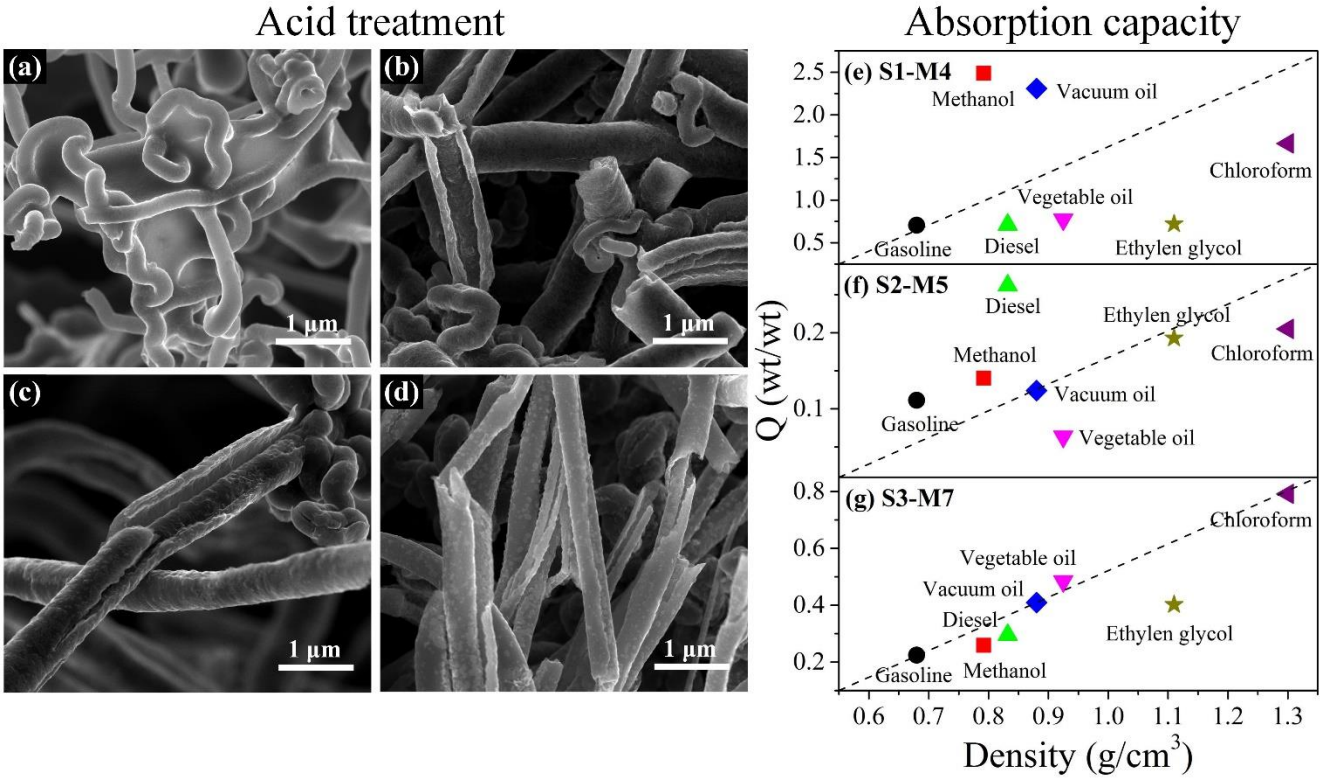

Figure 13: SEM images of N-CSTNs that were exposed to an acid treatment for one minute: **(a)** S1-M4, **(b)** S2-M5, **(c)-(d)** S3-M7. **(e)-(g)** Absorption capacities of N-CSTNs treated with acid. For the acid treatment, HNO_3/H_2SO_4 1:3 was used. Notable effects are observed on the surface morphology of N-CNS.